ARTICLE

OPEN

Check for updates

Submesoscale flows impact Agulhas leakage in ocean simulations

René Schubert [1✉], Jonathan Gula [2,3] & Arne Biastoch [1,4]

Agulhas leakage, the warm and salty inflow of Indian Ocean water into the Atlantic Ocean, is of importance for the climate-relevant Atlantic Meridional Overturning Circulation. South of Africa, the eastward turning Agulhas Current sheds Agulhas rings, cyclones and filaments of order 100 km that carry the Indian Ocean water into the Cape Basin and further into the Atlantic. Here, we show that the resolution of submesoscale flows of order 10 km in an ocean model leads to 40 % more Agulhas leakage and more realistic Cape Basin water-masses compared to a parallel non-submesoscale resolving simulation. Moreover, we show that submesoscale flows strengthen shear-edge eddies and in consequence lee cyclones at the northern edge of the Agulhas Current, as well as the leakage pathway in the region of the filaments that takes place outside of mesoscale eddies. This indicates that the increase in leakage can be attributed to stronger Agulhas filaments, when submesoscale flows are resolved.

[1] GEOMAR Helmholtz-Centre for Ocean Research Kiel, Kiel, Germany. [2] Univ Brest, CNRS, IRD, Ifremer, Laboratoire d'Océanographie Physique et Spatiale (LOPS), IUEM, Brest, France. [3] Institut Universitaire de France (IUF), Paris, France. [4] Christian-Albrechts-University Kiel, Kiel, Germany.
✉email: rschubert@geomar.de

Agulhas leakage (AL), the amount of warm and salty Indian Ocean water that enters the Atlantic, is of importance for the Atlantic Meridional Overturning Circulation[1–4], which impacts the global climate[5]. A prominent contribution to AL is provided by Agulhas rings[6], which are large mesoscale anticyclones irregularly shed by the retroflecting Agulhas Current (AC). They propagate northwestward through the Cape Basin into the Atlantic carrying the AC water with them. A smaller contribution to AL is provided by cyclonic mesoscale eddies and filaments that form at the northern edge of the AC[6–9]. In this study, we explore the impact of submesoscale dynamics of $\mathcal{O}$ (10 km) on the amount and pathways of AL. The strong eddy–eddy interactions in the Cape Basin are associated with the formation of submesoscale vortices along the eddy edges that strengthen the mesoscales[10,11], drive a water-mass exchange with the surrounding water[12–15] and thus mix Agulhas ring water out of the rings into the Cape Basin. Submesoscale flows are thus hypothesised to broaden the leakage pathway within the Cape Basin. Upstream, the strong horizontal shears between the AC and the waters on the shelf lead to mesoscale and submesoscale barotropic instabilities[7,16]. Both instabilities are associated with downstream-propagating meanders and shear-edge eddies that grow in size with time[7,9,16]. The shear-edge eddies are associated with surface-intensified warm plumes that occasionally propagate onto the shelf[7,16–18]. Moreover, the shear-edge eddy driven shelf-interior exchange impacts the ecosystems on the shelf, which is of importance for the South African fishery[7]. Submesoscale flows are hypothesised to strengthen the shear-edge eddies and thus to enhance the related shelf-interior exchange and the potentially associated AL. In contrast to the plumes, the shear-edge eddies are trapped between the continental slope and the AC accumulating cyclonic vorticity[7,18]. The vorticity leaks downstream towards the tip of the Agulhas Bank where it is absorbed by cyclones in the lee of the Agulhas Bank[9]. The lee cyclones can reach diameters of more than 200 km, detach from the slope and propagate southwestward into the Cape Basin, which potentially contributes to AL[9,12,19]. Moreover, the lee cyclones drive the formation of Agulhas filaments that contribute to AL by transporting AC waters northwestward into the Cape Basin[7,8,20]. A Global Drifter Programme surface drifter trajectory (Fig. 1), proves that AC waters can leak into the Atlantic by getting trapped in a shear-edge eddy, being transferred to a lee cyclone, leaving the lee cyclone in the Cape Basin and finally reach the Atlantic as part of the Good Hope Jet.

For this study, the effect of submesoscale flows onto AL is isolated by comparing the two numerical ocean simulations INALT60 and INALT20r that have been extensively validated against observations[10]. Both are global ocean simulations with a 1/20° grid refinement for the greater Agulhas region and differ only in that INALT60 has a secondary submesoscale-permitting 1/60° grid-refinement for the core Agulhas region ($0°E − 40°E$, $25°S − 45°S$). Besides the smaller horizontal and vertical grid-spacing, the effective dissipation and diffusion are also reduced in the domain of the secondary grid-refinement, contributing further to an increase in the effective resolution[21]. At around 28°E, the strength, variability, structure and extent of the Agulhas Current has been shown to be similar in both simulations and close to in situ observations[10]. This indicates that the secondary grid-refinement has only a small impact on the simulated large-scale dynamics of the northern Agulhas Current. In the southern Agulhas Current and the Cape Basin, INALT20r does not simulate submesoscale flows and showed deficiencies in the representation of in particular cyclonic mesoscales, while INALT60 simulates submesoscale and mesoscale flows, which compare very well statistically with satellite observations[10,11]. The presence or absence of submesoscale flows can also be seen in
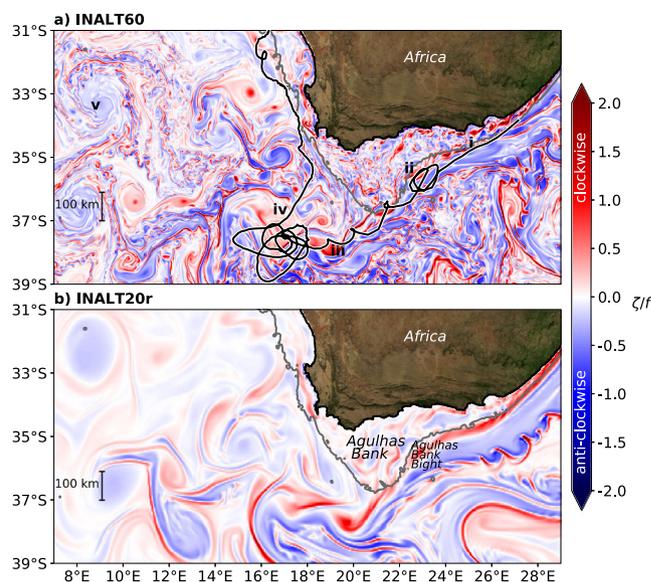

Fig. 1 Submesoscale flows in the Agulhas region. A zoom into snapshots of surface normalised relative vorticity (a measure of rotation) from INALT60 (**a**) and INALT20r (**b**) on model day July 18th 2012. The black-white line shows the trajectory of the Global Drifter Programme drifter number 101938 released on Feb 19th 2013. The extent of the Agulhas bank is highlighted with the 300 m isobath. Different dynamical features are marked: (i) submesoscale instabilities at the northern edge of the Agulhas Current (ii) a shear-edge cyclone in the Agulhas Bank Bight, (iii) a shear-edge cyclone southwest of the Agulhas Bank, (iv) a lee cyclone, and (v) an Agulhas ring with surrounding submesoscale vortices. For land areas a satellite picture is shown[49].

model snapshots of the surface normalised relative vorticity (Fig. 1).

The present study shows that the resolution of submesoscale flows leads to 40% more Agulhas leakage, more realistic Cape-Basin water-masses, as well as stronger shear-edge eddies and lee cyclones and a stronger Good Hope Jet. Further, we show that in particular the leakage pathway outside of mesoscale eddies is stronger when submesoscale flows are resolved and that it is located in the region of the Agulhas filaments. Combining, our results indicate that submesoscale flows are important for the formation of Agulhas filaments and the associated leakage.

Results
Agulhas leakage: hydrography, amount and eddy sojourn. Resolving submesoscale flows leads to a salinification and warming of the water-masses that enter the South Atlantic from the Cape Basin. In the upper 2500 m of the Agulhas ring path, in particular light South Atlantic Central Waters, South Atlantic Subtropical Mode Waters, and Antarctic Intermediate Waters show larger salinities in INALT60 compared to INALT20r (Fig. 2a). Moreover, the warmer water-masses increase in volume, while the colder decrease in volume, when submesoscale flows are resolved (numbers in Fig. 2a). The salinification and the warming point to a stronger contribution of Indian ocean waters to the Cape Basin water-mass properties and thus an increase of Agulhas leakage (AL). Further, a comparison to the reanalysis product GLORYS12V1[22] shows that the salinification and the warming improve the realism of the simulation (Fig. 2a). In particular the properties of the light South Atlantic Central Waters, the South Atlantic Subtropical Mode Waters and the Antarctic Intermediate Waters are more realistic when submesoscales are resolved. However, in INALT60 there is too much
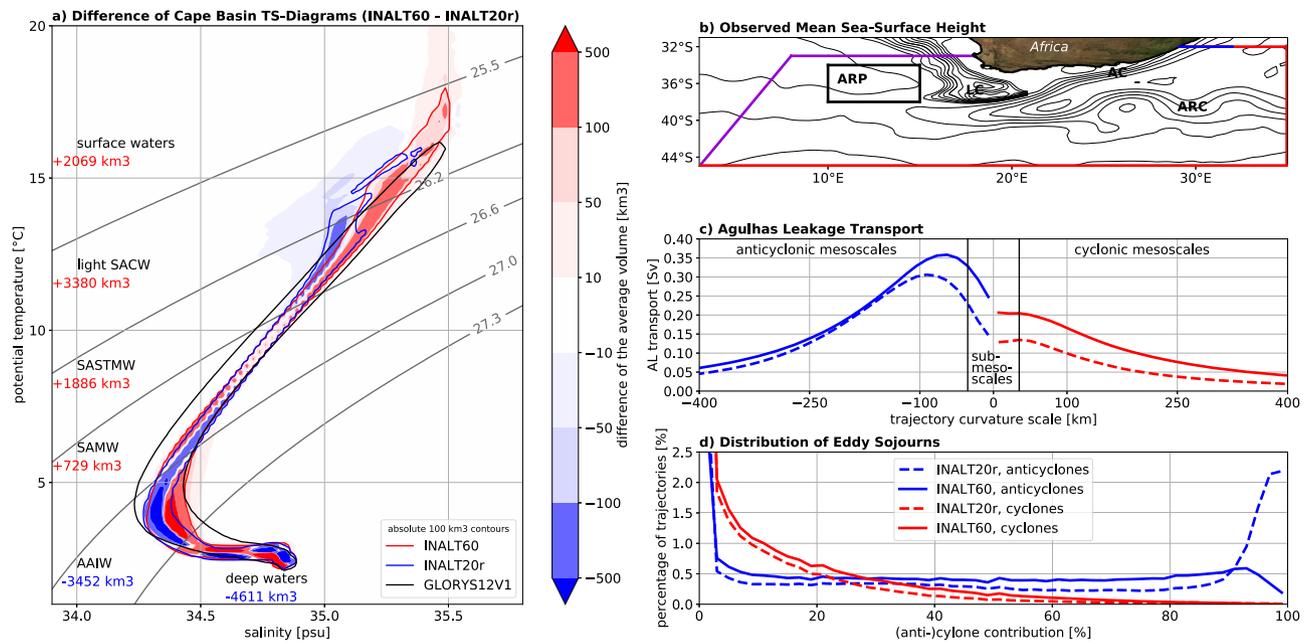
Fig. 2 Submesoscale flows salinify the ring path waters, enhance Agulhas leakage, in particular by strengthening non-anticyclonic leakage pathways, and lead to a stronger exchange of Agulhas rings with their surrounding. a Colours show the difference of INALT60 and INALT20r in the mean water volume associated with specific temperature-salinity properties in the upper 2500 m of the ring path (black box in **b**)) for the period 2012–2017. Red, blue and black lines show the respective absolute 100 km³ contours for INALT60, INALT20r and the reanalysis product GLORYS12V1[22]. Grey contours show potential density contours that define the water-masses of surface waters, light South Atlantic Central Water (SACW), South Atlantic Subtropical Mode Water (SASTMW), South Atlantic Mode Water (SAMW), Antarctic Intermediate Water (AAIW) and deep waters[50]. For each water-mass the sum over the difference of the respective volumes is given. **b** The 2012–2017 mean sea-surface height from the L4 CMEMS satellite altimetry product with a contour interval of 20 cm and southwest of Africa of 2 cm for the interval –30 cm to –10 cm to highlight the location of the time-mean lee cyclone (LC), the Agulhas Current (AC), the Agulhas Return Current (ARC) and the Agulhas Ring Path (ARP). Vsirtual Lagrangian particles are seeded within the AC at 32°S (blue) and contribute to Agulhas leakage if they reach the Good Hope Line (violet). The trajectories are also terminated, if they reach the red lines. For land areas a satellite picture is shown[49]. **c** The average Agulhas leakage transport decomposed into its contributions from trajectory curvature scales between 20°E and the Good Hope Line. **d** The distribution of the fraction of (anti-) cyclonic eddy sojourns for the leakage trajectories in the same region. **c** and **d** join the same legend.

volume of very light South Atlantic Central Waters (> 16°C) compared to the observations.

To investigate the AL and its pathways, we use a Lagrangian approach[23] that has been established[2,24–27]. Virtual particles are released in the simulated AC at 32°S (Fig. 2b, blue line). AL is then computed as the sum of the initial transports of all particles that reach the Good Hope Line west of Africa (Fig. 2b, violet line). Indeed, the mean AL transport increases from 8.5 Sv by about 40 % to 12.0 Sv, if submesoscale flows are resolved. The latter is closer to but smaller than the observational estimates of 15 Sv[28] and the newer value of 21 Sv[29], which has however been estimated for a different particle starting section that is known to be associated with higher AL. Note also that in another recent 1/20° simulation of the Agulhas region a higher average leakage transport of 9.7 Sv is found[30]. Possible reasons for the difference to the present 1/20° simulation are (among others) a larger nest domain, a smaller vertical resolution, and a longer integration length.

To reveal on which spatial scales and which rotational sense the AL particles move in the Cape Basin, and how this changes when submesoscale flows are resolved, the mean AL transport is shown for both simulations as a function of trajectory curvature scales in Fig. 2c. For every trajectory, the distribution of its trajectory curvature scale between 20°E and the Good Hope Line is multiplied by its transport, subsequently summed up over all trajectories and finally normalised by the number of release days. As expected, AL particles are associated more often with curvature scales smaller than 35 km, when submesoscales are

resolved. These motions occur both within and outside of mesoscale eddies. For curvature scales larger than 35 km, there is a pronounced increase on the cyclonic side, but only a small increase on the anticyclonic side, in particular for scales larger than 150 km. This indicates that the AL particles sojourn similarly often in anticyclonic mesoscale eddies (>150 km) in both simulations, but more often in cyclonic mesoscale eddies or outside the mesoscale eddies, when submesoscales are resolved. The integral of the whole distribution gives the mean AL transport. The increase of the total AL transport from INALT20r to INALT60 (3.6 Sv) can be split into an increase due to a 0.5 Sv submesoscale, a 1.1 Sv cyclonic mesoscale, a 0.5 Sv anticyclonic mesoscale and a 1.5 Sv straight contribution. The different contributions are obtained by integrating the difference of the two scale distributions between −35 km and +35 km (submesoscales), +35 km and +400 km (cyclonic mesoscales), −400 km and −35 km (anticyclonic mesoscales) and identifying the difference between the sum of the three integrals and the total AL transport to be the contribution of straight flows. The threshold of 35 km has been chosen, as this is the regional baroclinic Rossby radius of deformation[31], and 400 km as only rarely eddies with larger diameters have been detected in altimetry measurements of the region[10].

Here, an eddy-detection algorithm[32] is applied to investigate, where and how long the AL particles sojourn in cyclones and anticyclones in the Cape Basin, as well as how often they cross the eddy edges. As expected, the exchange through the eddy edges increases when submesoscale flows are resolved. Between 20°E
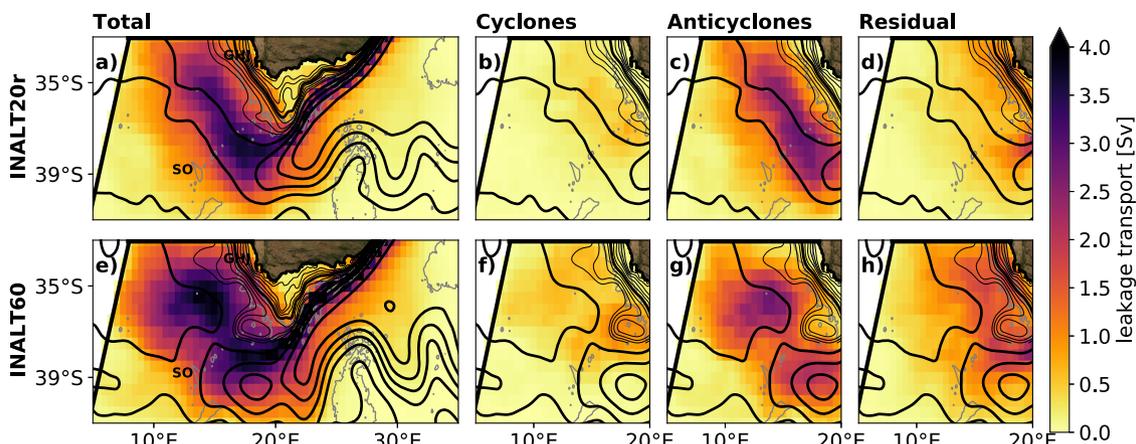
Fig. 3 Submesoscale flows broaden the Agulhas leakage pathway and enhance the leakage mainly by leading to a stronger Agulhas filament pathway.
Single-count cumulative transport of leakage particles normalised by the number of seeding days (colours) from INALT20r (**a–d**) and INALT60 (**e–h**) for the seeding period 2011–2014 and the full trajectories (**a**, **e**), as well as for leakage particles that sojourn in mesoscale cyclones (**b**, **f**), anticyclones (**c**, **g**) and outside of mesoscale eddies (**d**, **h**) within the Cape Basin. The bin size is 1/2° × 1/2°. Black contours show the 2012–2017 mean sea-surface height with contour intervals of 20 cm (thick), as well as of 2 cm between −30 cm and −10 cm north of 37.5°S (thin) to highlight the location and strength of the time-mean lee cyclone and the Good Hope Jet (GHJ). Black straight lines mark the position of the Good Hope Line. Grey contours show 300 m and 3000 m isobaths. The position of the Schmitt-Ott seamount (SO) is marked. For land areas a satellite picture is shown[49].

and the Good Hope Line, the average (normalised by the number of seeding days) transport of leakage particles through anticyclonic eddy edges is 100 Sv in INALT20r and 154 Sv in INALT60, and through cyclonic eddy edges it is 61 Sv in INALT20r and 102 Sv in INALT60. Consistently, a much smaller fraction of the AL particles stays most of the travel time (>90%) within anticyclones in INALT60 (Fig. 2d). In contrast to the anticyclones, only a very small fraction of AL particles stay longer than 50% of the time within cyclones in both simulations (Fig. 2d). The percentage of AL particles that stay >5% of the time in cyclones is slightly higher, when submesocales are resolved.

Agulhas leakage pathways. To investigate the submesoscale effect on the respective AL pathways, frequency maps of AL particles are shown for INALT20r and INALT60 for the full trajectories, as well as for AL particles that sojourn in mesoscale cyclones or anticyclones, and outside of mesoscale eddies within the Cape Basin (Fig. 3). In INALT20r, the AL pathway is narrow (Fig. 3a). The AL particles sojourn to a large extent in mesoscale anticyclones, but much less in mesoscale cyclones or outside of mesoscale eddies (Fig. 3b–d). If submesoscale flows are resolved, the AL pathway is much broader, in particular northwest of the seamount chain between the Schmitt-Ott seamount and the Agulhas bank (Fig. 3e). The majority of the AL particles also sojourns in mesoscale anticyclones, with similar frequencies than in the non-submesoscale resolving experiment but more particles sojourn in mesoscale cyclones and between the mesoscale eddies (Fig. 3f–h). Highest cyclonic frequencies are found northwest of the retroflection in a band with frequencies decreasing southwestward from a maximum in the lee of the Agulhas bank. The band is co-located with a minimum in the time-mean sea-surface height (SSH) in the lee of the bank and reduced SSH southwest of it, attributable to the formation and propagation of lee cyclones. This is not found in INALT20r, which shows that submesoscale flows strengthen lee cyclones and the related AL. However, the southwestward decreasing frequencies highlight that the AL particles are mainly mixed out of the lee cyclones and rarely cross the southwestern edge of the ring path within a lee cyclone. Compared to cyclonic AL frequencies, residual frequencies increase more strongly when submesoscales are resolved (Fig. 3d, h). Higher residual frequencies are found in particular between the central

ring path and the time-mean lee cyclone: the region where Agulhas filaments develop. Above the shelf, higher frequencies are found around 34°S in the region of the Good Hope Jet, which is stronger in INALT60 (identifiable by the distance of the SSH contours in Fig. 3). This may explain shorter average travel-times of AL particles from the seeding section to the Good Hope Line when submesoscales are resolved (235 days in INALT60 and 278 days in INALT20r). The drifter pathway shown in Fig. 1 is a typical example for a particle trajectory that reaches the Atlantic with the Good Hope Jet. Our results indicate that the resolution of submesoscale flows provides a near-shelf fast route into the South Atlantic by strengthening filaments, enhancing the mixing through the Agulhas ring and lee cyclone edges, as well as by strengthening the Good Hope Jet.

Agulhas cyclone formation. The presence of the time-mean SSH minimum in and southwest of the lee of the Agulhas bank in INALT60, and its absence in INALT20r (Fig. 3), show that submesoscale flows strengthen the lee cyclones. Moreover, the time-mean SSH minimum also exists with a similar amplitude in the mean observed SSH from L4 CMEMS (Fig. 2b) showing that the strengthening is necessary for a realistic representation of the lee cyclones in the simulation. This contributes to the very good agreement between INALT60 and observations in terms of scale distribution and numbers of strong cyclones in the Cape Basin, while INALT20r lacks strong cyclones[10].

We hypothesise that the strengthening of the lee cyclones, when submesoscale flows are resolved, can be attributed to the resolution of submesoscale barotropic instabilities at the northern edge of the AC. The resulting eddies have diameters of about 10 km and grow in size during their downstream propagation[16,33]. We hypothesise further that the growing features are dominant drivers of the formation of shear-edge eddies, which are downstream dominant drivers of the formation of lee cyclones. To test both hypotheses, we analyse the surface kinetic energy transfers through spatial and temporal scales when the AC is not in a strong meandering state (see Methods). At spatial scales of 10 km and 20 km, the energy transfer Π is mainly directed towards smaller scales (downscale) (Fig. 4a, b). In the open ocean, the downscale transfer is mainly confined to frontogenetic regions[11]. Strongest downscale fluxes occur at 10
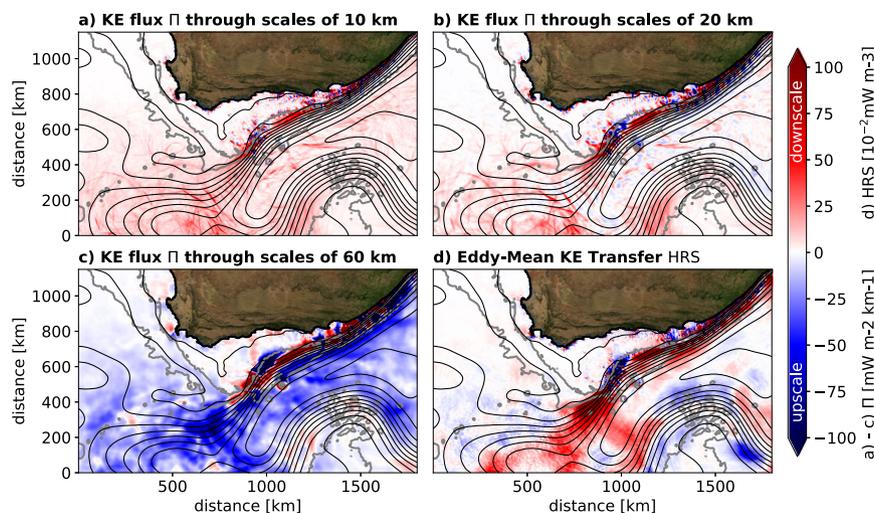
Fig. 4 Submesoscale flows strengthen shear-edge eddies and lee cyclones. The mean surface kinetic energy flux Π through horizontal scales of (**a**) 10 km, (**b**) 20 km, and (**c**) 60 km, as well as the mean surface eddy-mean kinetic energy transfer HRS **d** in INALT60. The quantities are computed based on 4-h mean output and averaged over periods when the Agulhas Current is not in a strong meandering state for the period 2012–2017. Negative values show upscale fluxes to larger scales and positive downscale fluxes to smaller scales. Black contours show the 2012–2017 mean SSH with an interval of 10 cm and grey contours the 300 m and 3000 m isobaths. For land areas, a satellite picture is shown[49].

km, 20 km and 60 km scales in a narrow band along the northern edge of the AC upstream of its separation from the continental slope (Fig. 4a–c). The narrow band is interrupted in the Agulhas Bank Bight, where upscale fluxes are found for scales of 20 km and 60 km. In the open ocean, the mean fluxes mainly change to upscale at scales between 20 km and 60 km. The results indicate that submesoscale instabilities upstream of the Agulhas Bank Bight extract kinetic energy from the AC and transfer it to scales smaller than 10 km. The resulting features grow in size and feed their kinetic energy upscale into the shear-edge eddies, in particular into the ones trapped in the Agulhas Bank Bight. Features that leak from the Agulhas Bank Bight are observed to accelerate and to be squeezed south of the tip of the Agulhas Bank[9]. This squeezing contributes to the downscale transfer found for the region downstream of the Agulhas Bank Bight. Further, the leaking features are occasionally small compared to the trapped shear-edge eddies[9]. The separation of the small features from the shear-edge eddy might provide a further contribution to the downscale transfer. Finally, a maximum of the upscale transfer through scales of 60 km southwest of the Agulhas Bank shows the strengthening of the lee cyclones by the absorption of the leaked features.

More evidence that shear-edge eddies are mainly driven by submesoscale upscale fluxes instead of large-scale barotropic instabilities is achieved by analysing the mean surface kinetic energy transfer from the time-mean to the time-varying flow through horizontal Reynolds stresses (HRS). Positive HRS is a common indicator for barotropic instabilities of a current[34,35]. The result, shown in Fig. 4d, reveals a very narrow band of positive HRS at the northern edge of the AC upstream of the Agulhas Bank Bight. The cross-stream extent of this band (≈ 40 km) gives a scale for the dominant barotropic instability indicating that the AC's northern edge mainly undergoes recurrent submesoscale barotropic instabilities.

Conclusion
In the present study, we systematically compare a submesoscale-permitting ocean simulation of the Agulhas current system to a parallel simulation that does not resolve submesoscale flows. We show that the resolution of submesoscale flows leads to an increase of Agulhas leakage by 40 % and more realistic Cape-

Basin water-masses. Resolving submesoscale barotropic instabilities at the northern edge of the Agulhas Current leads to a strengthening of shear-edge eddies, which leads further to a strengthening and thus better representation of lee cyclones west of the Agulhas Bank. However, a Lagrangian analysis indicates that the leakage particles trapped in lee cyclones are mainly mixed out of the eddies within the Cape Basin and only rarely reach the South Atlantic within the southwestward propagating eddies. Instead, leakage particles in the Cape Basin are found to sojourn more often outside of mesoscale eddies and to follow more often straight trajectory segments. As the leakage particles outside of eddies are found mainly in the region of the Agulhas filament development, we conclude that submesoscales enhance the leakage mainly by leading to stronger filaments, as a result of the stronger lee cyclones. Leakage particles also sojourn more often outside of mesoscale eddies as a direct effect of submesoscale instabilities along the eddy edges, which enhance the exchange of eddy waters with their surrounding. Moreover, leakage particles are more often found in the region of the Good Hope Jet that is stronger when submesoscale flows are resolved. The latter might be attributable to a better resolved bathymetry. Remarkably, leakage particles are rarely found to sojourn on the shelf of the Agulhas bank east of 20°E in both simulations (Fig. 3a). This indicates that warm plumes moving onto the shelf, that should be better represented when submesoscales are resolved, do not play a role for the leakage. A limitation of the study is the eddy-detection method that only detects larger eddies with a pronounced SSH signature and that assumes vertical eddy edges. Future research should focus on the vertical structure of Cape Basin eddies, submesoscale flows and Agulhas leakage, as well as on the role of smaller mesoscale eddies and small-scale topographic features in the leakage dynamics. For example, the effect of small-scale topography on the splitting of Agulhas rings and its consequences for the Agulhas leakage should be investigated. While we do not expect an effect on the total amount of Agulhas leakage, we expect an effect on the leakage pathways. A further limitation of the study is that submesoscale processes are only partially resolved by the model. Future model simulations and observations with a higher capability of resolving submesoscale flows can shed light on the impact of even smaller scale flows onto the Agulhas leakage. As the Agulhas Leakage is of

importance for the climate-relevant Atlantic Meridional Over-turning Circulation, the present study indicates that submesoscale flows in the Agulhas region are important for the global climate. In the future, the respective effects could be identified with longer submesoscale resolving simulations that are currently not feasible. Subsequently, a parameterisation of these effects need to be developed for climate models, as even the latest eddy-active 1/4° CMIP6 climate models do not resolve submesoscale Agulhas dynamics at all.

Methods

The model experiments. The two numerical model experiments, analysed for this study, are validated against observations and described in detail in ref. [11]. Here, only a short summary is provided. Both ocean-only configurations use a global 1/4° grid and a grid refinement down to a 1/20° grid-spacing that extends from 50°S, 20°W to 6°S, 70°W and covers the eastern half of the South Atlantic Ocean and the western half of the South Indian Ocean. Both experiments are initialised with fields from the last time-step of a 30 year spin-up from 1980 to 2009 that has been integrated with this nested configuration under COREv2 forcing[36] using 46 vertical z-levels. In contrast, the two simulations here use JRA55-do v1.3 forcing[37], which is associated with higher temporal and spatial resolution, and 120 vertical z-levels. The simulations are integrated till the end of 2017. The first experiment, performed with the above described configuration, is referred to INALT20r.L120.HighDiff[10]. The abbreviation denotes that the model configuration is part of the INALT family[27], the horizontal resolution of the nest with the highest resolution (20 for 1/20°), that a reduced nested domain is used (r), the number of vertical levels (L120) and the diffusion and dissipation setting (explicit diffusion and dissipation and TVD/EEN discretisation schemes (HighDiff) or no explicit diffusion and dissipation and UBS schemes (LowDiff). In this study it is named for simplicity INALT20r. INALT20r resolves almost no submesoscales in the Agulhas region. The second parallel experiment, INALT60.L120.LowDiff (short INALT60), is associated with exactly the same configuration, but with a secondary nest for the core Agulhas region (45°S, 0°W to 25°S, 40°W) down to a 1/60° grid-spacing. Within the second nest, INALT60 resolves a large portion of the submesoscale spectrum and compares well to observations at all simulated scales[10].

Normalised relative vorticity. The normalised relative vorticity is given by ζ/f, where $\zeta = v_x - u_y$ is the vertical component of the relative vorticity (with the zonal velocity component u, the meridional velocity component v, the zonal Cartesian axis x and the meridional axis y) and $f = 2\Omega \sin(2\pi \frac{\theta}{360°})$ is the planetary vorticity (with the angular speed of the Earth $\Omega = \frac{2\pi}{86400}$ s-1 and the latitude θ). Partial derivatives of a with respect to b are written throughout this paper as $\frac{\partial a}{\partial b} = a_b$.

Mesoscale eddy detection. For the detection of mesoscale eddies and their edges, an eddy-detection algorithm[32] is applied to the temporally detrended and domain-average reduced daily-mean sea-surface height anomalies interpolated onto a 1/4° grid for the region 1°E–25°E, 26°S–44°S. The sea-surface height anomalies are scanned for thresholds between 1 m (–1 m) to –1 m (1 m) with an increment of 1 cm. If a connected set of 8–1000 pixels with sea-surface height anomalies below (above) the current threshold has a local minimum (maximum) with an amplitude of at least 1 cm, as well as a maximum pixel distance of 700 km, the pixel set is identified to be a cyclone (anticyclone) and its interior pixels are removed from the further detection.

Lagrangian particle tracking for the computation of Agulhas leakage. Every model day, virtual particles are released in the simulated AC at a 300-km-long section at 32°S (Fig. 1, inlay, blue line) with ARIANE[23]. At the centre of each vertical grid-cell, one particle is released at 12 AM. The current transport through the respective grid cell is tagged to each particle, while the particles follow the daily 4D daily-mean flow field. If the current transport through a grid-cell exceeds 0.01 Sv, the grid-cell is divided into four similar sized sub-cells and two times four particles are released at the centres of the sub-cells at 6 a.m. and 6 p.m. (each associated with 1/8 of the total transport). If the particles reach the Good Hope Line within 3 years, the respective trajectories are terminated and their transports contribute to AL. Trajectories are further terminated, if they reach the boundaries at 45°S, 35°E or 32°S. For this study, particles that are released in the years 2011–2014 are analysed.

Trajectory curvature scale. The curvature of a trajectory is given by $\kappa = (x'y'' - x''y')/(x'^2 + y'^2)^{\frac{3}{2}}$[12], where x and y are the Cartesian coordinates of the particle positions. Dashes mark temporal derivatives. The Cartesian distance for the derivatives is computed using the Haversine formula. The reciprocal of the curvature is the curvature radius $r = 1/\kappa$. The curvature scale is defined to be the respective diameter, with the opposite sign $(-2r)$. A positive (negative) curvature scale corresponds to a cyclonic (anticyclonic) movement.

Identifying periods when the Agulhas current is not in a strong meandering state. Downstream-propagating large meanders of the AC develop in the Natal Bight and are thus referred to as Natal Pulses[38]. Natal Pulses occasionally trigger the shedding of Agulhas rings and disturb the evolution of the shear-edge, as well as lee cyclones[9,39,40]. Here, Natal Pulses are identified at around 28°E along the Agulhas Current Timeseries (ACT) section[41] based on a common methodology[42] as events, where the offshore-distance of the maximum of the vertically integrated southwestward cross-section transport is more than one standard deviation larger than average. To account for the variability regarding the short time-scales, which is stronger in INALT60 compared to INALT20r, a further condition is added on the duration of the event. Here, periods with Natal Pulses at the ACT section are identified as periods, when the offshore-distance of the maximum of the south-westward vertical integrated cross-section transport exceeds the average (i) for >15 consecutive days and (ii) by one standard deviation for at least one day of this period. The identified periods agree with those identified by eye in animations of the SSH. Events that fulfil only the second condition are not attributable to Natal Pulses. Based on the SSH evolution along the northern edge of the AC, it is further identified that Natal Pulses need on average about 100 days from the ACT section to the retroflection. Thus, we define Natal Pulse periods as 100 day periods starting with the detection of a Natal Pulse at the ACT section. Besides the Natal Pulses, also other events can strongly disturb the AC in the region of the shear-edge eddy formation. In INALT60, at the end of the model year 2013, a cyclone detached from the ARC's first meander trough, travelled northwestward and lead to a substantial meandering of the southern AC between December 22nd 2013 and February 11th 2014. In this period, the AC is also considered to be in a strong meandering state.

Kinetic energy transfer through temporal and spatial scales. The kinetic energy transfer from the time-mean flow to the time-varying flow by horizontal Reynolds stresses is computed as HRS $= -\rho_0[\overline{u'u'}\overline{u}_x + \overline{u'v'}(\overline{u}_y + \overline{v}_x) + \overline{v'v'}\overline{v}_y]$[34,35], where $\rho_0 = 1024$ kg m^{-3} is the reference density. Overbars denote the mean over the investigated period and dashes deviations from that mean. Positive HRS is an indicator of barotropic instability[35,43]. The kinetic energy flux (the rate of kinetic energy transfer) from currents with spatial scales larger than a specific scale L to currents with scales smaller than L is computed as $\Pi = -\rho_0[(\overline{u^2} - \overline{u}^2)\overline{u}_x + (\overline{uv} - \overline{u}\overline{v})(\overline{u}_y + \overline{v}_x) + (\overline{v^2} - \overline{v}^2)\overline{v}_y]$[44–46], where the over-bars denote convoluted fields using an area-normalised two-dimensional top-hat convolution kernel of diameter L. The definition of the scale kinetic energy flux, in distinction to the spatial transfer of kinetic energy, is associated with a gauge freedom[47]. Here, we use a separation of transfers across scales and in space that has been suggested to be a suitable one due to its Galilean invariance[47]. Details on the application of this method to the INALT60 output are described by ref. [11]. The respective code is available on GitHub[48].

Data availability

This study bases on ocean model output data from two simulations that are described in detail in the literature including the model input data[10,27]. The size of the model output data is too large for an upload. The data to reproduce the plots of this study can be accessed with the following link: https://hdl.handle.net/20.500.12085/c572cde8-a82c-4c2d-9bd7-288dfc8f1939. The trajectory of the drifter shown in Fig. 1 can be accessed here: https://www.aoml.noaa.gov/phod/gdp/data.php. The black contour line in Fig 2a has been computed using E.U. Copernicus Marine Service Information. The respective GLORYS12V1 data can be downloaded here: https://resources.marine.copernicus.eu/?option=com_csw&view=details&product_id=GLOBAL_REANALYSIS_PHY_001_030. The sea-surface height data used for Figure 2b can be accessed here: https://resources.marine.copernicus.eu/?option=com_csw&view=details&product_id=SEALEVEL_GLO_PHY_L4_REP_OBSERVATIONS_008_047.

Code availability

The code to reproduce the figures of this study is provided in the jupyter notebook produce_plots.ipynb (https://hdl.handle.net/20.500.12085/c572cde8-a82c-4c2d-9bd7-288dfc8f1939). The code to compute the scale kinetic energy flux using coarse-graining is available at https://doi.org/10.5281/zenodo.4476094.

References

1. Weijer, W., de Ruijter, W. P., Sterl, A. & Drijfhout, S. S. Response of the Atlantic overturning circulation to South Atlantic sources of buoyancy. *Glob. Planet. Change* **34**, 293–311 (2002).
2. Biastoch, A., Böning, C. W. & Lutjeharms, J. Agulhas leakage dynamics affects decadal variability in Atlantic overturning circulation. *Nature* **456**, 489 (2008).

3. Biastoch, A. et al. Atlantic multi-decadal oscillation covaries with Agulhas leakage. *Nat. Commun.* **6**, 10082 (2015).

4. Lübbecke, J. F., Durgadoo, J. V. & Biastoch, A. Contribution of increased Agulhas leakage to tropical Atlantic warming. *J. Clim.* **28**, 9697–9706 (2015).

5. Zhang, R. et al. A review of the role of the Atlantic meridional overturning circulation in Atlantic multidecadal variability and associated climate impacts. *Rev. Geophys.* **57**, 316–375 (2019).

6. De Ruijter, W. et al. Indian-Atlantic interocean exchange: Dynamics, estimation and impact. *J. Geophys. Res.: Oceans* **104**, 20885–20910 (1999).

7. Lutjeharms, J., Catzel, R. & Valentine, H. Eddies and other boundary phenomena of the Agulhas Current. *Cont. Shelf Res.* **9**, 597–616 (1989).

8. Lutjeharms, J. & Cooper, J. Interbasin leakage through Agulhas current filaments. *Deep Sea Res. Part I: Oceanogr. Res. Papers* **43**, 213–238 (1996).

9. Lutjeharms, J., Boebel, O. & Rossby, H. Agulhas cyclones. *Deep Sea Res. Part II: Top. Stud. Oceanogr.* **50**, 13–34 (2003).

10. Schubert, R., Schwarzkopf, F. U., Baschek, B. & Biastoch, A. Submesoscale impacts on mesoscale Agulhas dynamics. *J. Adv. Model. Earth Syst.* **11**, 2745–2767 (2019).

11. Schubert, R., Gula, J., Greatbatch, R. J., Baschek, B. & Biastoch, A. The submesoscale kinetic energy cascade: mesoscale absorption of submesoscale mixed layer eddies and frontal downscale fluxes. *J. Phys. Oceanogr.* **50**, 2573–2589 (2020).

12. Boebel, O. et al. The Cape Cauldron: a regime of turbulent inter-ocean exchange. *Deep Sea Res. Part II: Top. Stud. Oceanogr.* **50**, 57–86 (2003).

13. Van Aken, H. et al. Observations of a young Agulhas ring, Astrid, during MARE in March 2000. *Deep Sea Res. Part II: Top. Stud. Oceanogr.* **50**, 167–195 (2003).

14. Capuano, T. A., Speich, S., Carton, X. & Blanke, B. Mesoscale and submesoscale processes in the Southeast Atlantic and their impact on the regional thermohaline structure. *J. Geophys. Res: Oceans* **123**, 1937–1961 (2018).

15. Sinha, A., Balwada, D., Tarshish, N. & Abernathey, R. Modulation of lateral transport by submesoscale flows and inertia-gravity waves. *J. Adv. Model. Earth Syst.* **11**, 1039–1065 (2019).

16. Tedesco, P., Gula, J., Ménesguen, C., Penven, P. & Krug, M. Generation of submesoscale frontal eddies in the Agulhas Current. *J. Geophys. Res. Ocean.* **124**, 7606–7625 (2019).

17. Schumann, E. & van Heerden, I. L. Observations of agulhas current frontal features south of africa, october 1983. *Deep Sea Res. Part A. Oceanogr. Res. Papers* **35**, 1355–1362 (1988).

18. Lutjeharms, J., Penven, P. & Roy, C. Modelling the shear edge eddies of the southern Agulhas Current. *Cont. Shelf Res.* **23**, 1099–1115 (2003).

19. Penven, P., Lutjeharms, J., Marchesiello, P., Roy, C. & Weeks, S. Generation of cyclonic eddies by the Agulhas Current in the lee of the Agulhas Bank. *Geophys. Res. Lett.* **28**, 1055–1058 (2001).

20. Whittle, C., Lutjeharms, J., Rae, D. & Shillington, F. Interaction of Agulhas filaments with mesoscale turbulence: a case study. *South African J. Sci.* **104**, 135–139 (2008).

21. Soufflet, Y. et al. On effective resolution in ocean models. *Ocean Model.* **98**, 36–50 (2016).

22. Global Monitoring and Forecasting Center. GLORYS12V1-Global Ocean Physical Reanalysis Product, E.U. Copernicus Marine Service Information [Data set]. Available at https://resources.marine.copernicus.eu/?option=com_csw&view=details&product_id=GLOBAL_REANALYSIS_PHY_001_030 (2018) (Accessed: 10th June 2021).

23. Blanke, B. & Raynaud, S. Kinematics of the Pacific equatorial undercurrent: An Eulerian and Lagrangian approach from GCM results. *J. Phys. Oceanogr.* **27**, 1038–1053 (1997).

24. Speich, S., Blanke, B. & Madec, G. Warm and cold water routes of an OGCM thermohaline conveyor belt. *Geophys. Res. Lett.* **28**, 311–314 (2001).

25. Durgadoo, J. V., Loveday, B. R., Reason, C. J., Penven, P. & Biastoch, A. Agulhas leakage predominantly responds to the Southern Hemisphere westerlies. *J. Phys. Oceanogr.* **43**, 2113–2131 (2013).

26. Wagner, P., Rühs, S., Schwarzkopf, F. U., Koszalka, I. M. & Biastoch, A. Can Lagrangian tracking simulate tracer spreading in a high-resolution Ocean General Circulation Model? *J. Phys. Oceanogr.* **49**, 1141–1157 (2019).

27. Schwarzkopf, F. U. et al. The INALT family–a set of high-resolution nests for the Agulhas Current system within global NEMO ocean/sea-ice configurations. *Geosci. Model Dev.* **12**, 3329–3355 (2019).

28. Richardson, P. L. Agulhas leakage into the Atlantic estimated with subsurface floats and surface drifters. *Deep Sea Res. Part I: Oceanogr. Res.Paper.* **54**, 1361–1389 (2007).

29. Daher, H., Beal, L. M. & Schwarzkopf, F. U. A new improved estimation of Agulhas leakage using observations and simulations of Lagrangian floats and drifters. *J. Geophys. Res.: Ocean.* **125**, e2019JC015753 (2020).

30. Schmidt, C., Schwarzkopf, F. U., Rühs, S. & Biastoch, A. Characteristics and robustness of Agulhas leakage estimates: an inter-comparison study of lagrangian methods. *Ocean Sci.* **17**, 1067–1080 (2021).

31. Chelton, D. B., Deszoeke, R. A., Schlax, M. G., El Naggar, K. & Siwertz, N. Geographical variability of the first baroclinic Rossby radius of deformation. *J. Phys. Oceanogr.* **28**, 433–460 (1998).

32. Chelton, D. B., Schlax, M. G. & Samelson, R. M. Global observations of nonlinear mesoscale eddies. *Prog. Oceanogr.* **91**, 167–216 (2011).

33. Krug, M., Swart, S. & Gula, J. Submesoscale cyclones in the Agulhas current. *Geophys. Res. Lett.* **44**, 346–354 (2017).

34. Harrison, D. & Robinson, A. Energy analysis of open regions of turbulent flows-Mean eddy energetics of a numerical ocean circulation experiment. *Dynam. Atmos. Ocean.* **2**, 185–211 (1978).

35. Storch, J.-Sv et al. An estimate of the Lorenz energy cycle for the world ocean based on the STORM/NCEP simulation. *J. Phys. Oceanogr.* **42**, 2185–2205 (2012).

36. Griffies, S. M. et al. Coordinated ocean-ice reference experiments (COREs). *Ocean Model.* **26**, 1–46 (2009).

37. Tsujino, H. et al. JRA-55 based surface dataset for driving ocean–sea-ice models (JRA55-do). *Ocean Model.* **130**, 79–139 (2018).

38. Lutjeharms, J. & Roberts, H. The Natal pulse: an extreme transient on the Agulhas Current. *J. Geophys. Res.: Ocean.* **93**, 631–645 (1988).

39. de Ruijter, W. P., Van Leeuwen, P. J. & Lutjeharms, J. R. Generation and evolution of Natal Pulses: solitary meanders in the Agulhas Current. *J. Phys. Oceanogr.* **29**, 3043–3055 (1999).

40. van Leeuwen, P. J., de Ruijter, W. P. & Lutjeharms, J. R. Natal pulses and the formation of Agulhas rings. *J. Geophys. Res.: Ocean.* **105**, 6425–6436 (2000).

41. Beal, L. M., Elipot, S., Houk, A. & Leber, G. M. Capturing the transport variability of a western boundary jet: Results from the Agulhas Current Time-Series Experiment (ACT). *J. Phys. Oceanogr.* **45**, 1302–1324 (2015).

42. Krug, M., Tournadre, J. & Dufois, F. Interactions between the agulhas current and the eastern margin of the agulhas bank. *Cont. Shelf Res.* **81**, 67–79 (2014).

43. Gula, J., Molemaker, M. J. & McWilliams, J. C. Topographic generation of submesoscale centrifugal instability and energy dissipation. *Nat. Commun.* **7**, 12811 (2016).

44. Leonard, A. Energy Cascade in Large-Eddy Simulations of Turbulent Fluid Flows, in *Advances in Geophysics*, Vol. 18, 237–248 (Elsevier, F.N. Frenkiel and R.E. Munn, 1975).

45. Germano, M. Turbulence: the filtering approach. *J. Fluid Mechan.* **238**, 325–336 (1992).

46. Eyink, G. L. Locality of turbulent cascades. *Phys. D: Nonlinear Phenom.* **207**, 91–116 (2005).

47. Aluie, H., Hecht, M. & Vallis, G. K. Mapping the energy cascade in the North Atlantic Ocean: the coarse-graining approach. *J. Phys. Oceanogr.* **48**, 225–244 (2018).

48. Schubert, R. & Rath, W. reneschubert/keflux: Computing the oceanic kinetic energy flux across spatial scales using coarse-graining (Version v1.0.0). *Zenodo*, https://doi.org/10.5281/zenodo.4476094 (2021).

49. Stöckli, R., Vermote, E., Saleous, N., Simmon, R. & Herring, D. *the Blue Marble next Generation-a True Color Earth Dataset Including Seasonal Dynamics from Modis*. (NASA Earth Observatory, 2005).

50. Donners, J., Drijfhout, S. & Hazeleger, W. Water mass transformation and subduction in the South Atlantic. *J. Phys. Oceanogr.* **35**, 1841–1860 (2005).

Author contributions
R.S. and A.B. designed the study and the experimental strategy. R.S. performed the numerical model simulations, developed and executed the analyses, produced all figures and wrote the text. A.B. and J.G. contributed to the analysis, the discussion of the results, and the writing of the manuscript.

Competing interests
The authors declare no competing interests.

Additional information
Supplementary information The online version contains supplementary material available at https://doi.org/10.1038/s43247-021-00271-y.

Correspondence and requests for materials should be addressed to René Schubert.

Peer review information *Communications Earth & Environment* thanks Isabelle Ansorge and the other, anonymous, reviewer(s) for their contribution to the peer review of this work. Primary handling editors: Regina Rodrigues, Heike Langenberg. Peer reviewer reports are available.

Reprints and permission information is available at http://www.nature.com/reprints

Publisher's note Springer Nature remains neutral with regard to jurisdictional claims in published maps and institutional affiliations.